APPLICABILITY OF AN HERTZIAN-TYPE CONTACT MODEL FOR WHEEL-RAIL PAIRINGS AS SEEN BY AN IMPROVED POST-PROCESSING SCHEME FOR ULTRASONIC DATA

Bruno Leban[1], Matteo Russo[1], Manuel Freudenberger[2], Andreas Trausmuth[2], Markus Varga[2], and András Vernes[2]

[1] *Department of Mechanical, Chemical and Materials Engineering, University of Cagliari, Via Marengo, 2 – 09123, Cagliari, Italy*

[2] *AC2T research GmbH, Viktor-Kaplan-Straße 2/C, 2700, Wiener Neustadt, Austria*

Corresponding author Andras Vernes, Prof., AC2T research GmbH, Viktor Kaplan-Straße 2, 2700 Wiener Neustadt, AUSTRIA., Tel.: +43 2622 81600-360, E-mail: andras.vernes@ac2t.at, https://orcid.org/0000-0003-2750-9811

Abstract

The contact between wheel and rail crucially affects the management of railways, since the vehicle dynamics, safety, and performance, for example, are all dependent on this. Therefore, in this contribution the load-dependence of nominal contact area – a broadly not considered aspect of the wheel-rail contacts within the literature – is addressed. We are applying an ultrasonic technique for the detection of the contact zone and an improved post-processing scheme for the measured ultrasonic reflection data. Accordingly, we found that the nominal contact area shows a power-law dependence on load which only on average is predicted by the elliptical Hertzian contact theory.

Keywords:

wheel-rail contact ;
ultrasound technique ;
load-dependent nominal contact area ;
numerical simulations ;

1 Introduction

Railway transport has gained significant attention in recent years due to its energy efficiency and its potential to decrease CO_2 emissions in transport. However, there still exist significant technical challenges that can affect the capability of railway to provide cheap and reliable long-range transport. In particular, recent trends toward higher speeds and increased loads lead to more severe contact conditions for the wheel-rail system, increasing wear and component damage due to fatigue-related mechanisms. In particular, damage mechanisms such as pitting or rolling contact fatigue (RCF) or wear, are aggravated by high loads concentrated on the small real contact areas characteristically of Hertzian contacts. Due to the previous, proper characterisation of the geometry and extent of contact areas in the wheel-rail systems is necessary for the evaluation and prediction of component damage by fatigue-related mechanisms, e.g., as functions of used materials. These characteristics of the contact in case of worn wheel-rail pairings, allow one also to draw conclusions on the sources of the observed wear in terms of the occurring contact pressure and tension. This information in turn can then be used to reduce the wear of wheel and rail with a proper pairing of materials and hence increase their lifetime.. Several techniques have been used to this end, ranging from optical to electrical conductivity measurements, although higher degrees of precision are still necessary. In recent years, the measurement of contact interfaces by means of ultrasonic techniques has become widespread in rail applications due to their non-destructive, non-intrusive characteristics. In this context, the pulse-echo technique measuring the reflection of high-frequency ultrasonic waves on the wheel-rail interface has become a standard in railway applications [1].

In fact, the study of the static contact between wheel and rails by means of the ultrasonic technique is well established in the literature. The first application of the ultrasonic technique by using a set-up commonly employed in non-destructive testing analysis for the assessment of the size and shape of the contact area is described in [2] and good agreement with the values predicted by the Hertzian theory of contact was achieved. In the same paper, they presented an approach for measuring the pressure distribution at the contact interface by establishing an empirical relationship between the contact pressure and the measured ultrasound pulse reflection coefficient. In a subsequent work [3], the authors refined the experimental method by including in the calibration procedure the results of a finite element model. In [4] is described the implementation of the Tattersall's model [5] to measure the contact pressure in wheel-rail system by establishing an empirical relationship between the contact stiffness and the pressure at the contact interface. In order to increase the accuracy of measurements, data post-processing techniques were implemented in [6]. In particular, the authors successfully used the direct deconvolution of the reflection maps by an approximate impulse response of the ultrasonic transducer in order to deal with the blurring effect decreasing measurement accuracy. Similarly, the application of the Wiener deconvolution for the enhancement of reflection maps is presented in [7]. In such work, the transducer impulse response was determined by the ASTM E1065 test [8].

The surface quality of railway components has also been taken into account in the available literature, in order to account for the effects of roughness and wear. The contact between wheel and rail elements in which defects as holes and grooves were induced was investigated in [9], showing the suitability of the ultrasonic technique in detecting irregularities potentially present at the contact interface. Further investigations on the contact between wheel and rail in the presence of sub-surface defects have been reported in [10]. Additionally, the ultrasonic method was used for studying the influence of wear in the wheel-rail contact on size and shape of

the contact area and pressure distribution at the interface considering unused, sand damaged, and worn wheel and rail elements [11].

In recent studies, array transducers have been employed for the characterization of dynamic contact in wheel-rail systems. The contact between wheel flange and rail gauge corner, both in static and dynamic conditions are presented in [12]. By employing a linear array transducer, the authors investigated the influence of increasing tractive forces on contact conditions by measuring the interfacial contact stiffness. Furthermore, they observed that by carrying cyclic rolling tests, a change in surface topography is followed by an increase in contact stiffness, suggesting that an increase in real area occurs during wheel-rail operations. Further results on the dynamic contact patch evolution at low rolling speeds have been summarised in [13].

In spite of the published work, the proper modelling of the propagation of ultrasonic pulses across the wheel-rail interface is an issue not satisfactorily solved so far. Previous attempts by Tattersall [5] treated the contact interface as a weightless layer of springs connecting two ideally elastic media, leading to the definition of the reflection coefficient for a normally incident wave as a function of its frequency, the acoustic impedances of the materials and the contact stiffness. Extending Tattersall's approach, other authors proposed solutions for the problem of transmission and reflection of ultrasonic waves through imperfectly bonded interfaces, covering the general case of skew incident primary and share waves [14], and taking into account the effect of interface ultrasound attenuation [15].

However, from the previous is it clear that improvement in the context of measurement processing is needed in order to obtain accurate data on stresses and contact area for the wheel-rail system. In an effort to improve this situation, an innovative algorithm for the determination of the contact area as a function of applied load has been developed in this work and compared with the results of FEM simulations performed on the wheel-rail system.

2 Basic concepts

In this section, our ultrasound technique it is detailed, measuring the nominal contact area via an areal mapping of the reflection coefficient, which in turn properly exploits the sensitivity of ultrasound reflection on the occurrence of solid-solid contacts between two interacting rough surfaces. As it will be seen, a carefully selected threshold for the reflection coefficient enables to include more than 99% of the reflection data originated from the solid-solid contacts. This yields enough accuracy, to measure the nominal (and not real) contact area. The so resulting accuracy for the nominal contact area will be later also confirmed by our numerical simulations, see Section 4, performed using the finite element method (FEM) which is here also briefly summarized.

2.1 Ultrasonic measurement

The static contact between wheel-rail specimens was experimentally investigated by applying ultrasonic reflectometry. An ultrasonic pulse emitted in a broad spectrum of frequencies by an ultrasonic transducer is sent to the contact interface. As waves strike the surface of separation between two media, part of the incident wave is transmitted, and part is reflected [16]. For a perfectly bonded contact pair, the portion of reflected signal indicated as reflection coefficient R can be expressed as follow:

$$R = \frac{Z_2 - Z_1}{Z_2 + Z_1} \tag{1}$$

where Z_1 and Z_2 are the acoustic impedances given by the product of materials' density and speed of sound. When the acoustic impedances of the contacting bodies are the same, as in the case of wheel-rail contact, the ultrasonic wave is totally transmitted at the contact interface (i.e., R=0). On the contrary, the waves are totally reflected at a solid-gas interface.

In the case of dry contact, the contact interface can be figured as a distribution of contacting asperities surrounded by air gaps formed by the matching of the two rough surfaces. Owing to the presence of the air gaps acting as reflectors, the portion of reflected and transmitted wave varies locally. As the contact stress increases, the number and size of contact spots grows, therefore the amount of transmitted energy increases and, simultaneously, the reflected amount decreases. Figure 1 illustrates this phenomenon, which is measured by analysing the amplitude variations of the reflected. The measurement of the amplitude of the ultrasonic signal reflected from different points of the contact region allows to obtain information on size and shape of the contact patch and the contact pressure among it. The graphic representation of the spatial distribution of the reflection coefficient will be referred to as the contact map. The resolution of ultrasonic transducers typically employed in the analysis of contact problems does not allow to resolve the contact between single asperities. Therefore, the reflected signal is the net result of the waves-air gaps interactions over the area irradiated by the ultrasonic beam. As pointed out in [17], the nature of these interactions depends on the relative size between air gaps and wavelength of the ultrasonic waves, and the suitable condition for studying the contact is the regime of long wavelengths.

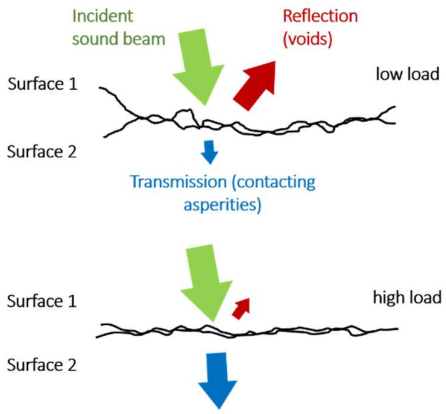

Figure 1 - Selective transmission and reflection of ultrasonic waves from a rough interface.

2.1.1 Reflection coefficient

In this section, two approaches for the measuring of the reflection coefficient are proposed.

On approach consists in defining the reflection coefficient at each measured point as the ratio between the amplitude H_i of the signal reflected by the contact interface while a certain load is applied and the amplitude of the signal reflected at the same point before the application of the load, H_{0i}. Thus, the reflection coefficient is given as:

$$R_i = \frac{H_i}{H_{0_i}} \tag{1}$$

The result of the pixel-by-pixel division between a contact map and the map of the same region before the application of the load is shown in Figure 2.

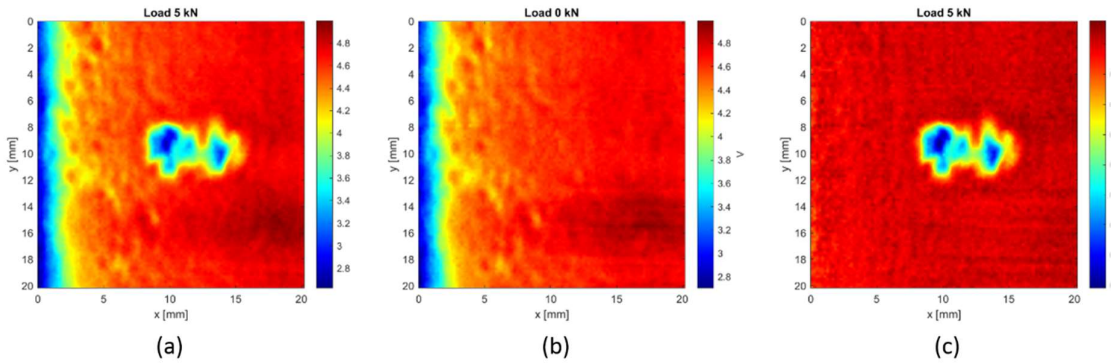

Figure 2 – (a) Contact map at 5kN; (b) Signal reflected before the application of the load; (c) Reflection map at 5kN.

Since an accurate spatial match between the reference measurement and the subsequent contact maps is made, the gradient due to the reflection of the ultrasonic beam from a not perpendicular surface is eliminated (see Figure 2 (c)). Because of the deformation of the specimens under the applied load, small shifts of the scan area may occur.

The second approach consists in dividing the amplitude of the reflected signal H_i by a single value measured where no contact occurs. Thus, reflection coefficient at each measured point is defined as:

$$R_i = \frac{H_i}{\overline{H}_0} \tag{2}$$

where $\overline{H}_0$ is given by the averaging of different measurements belonging to the steel-air interface.
This approach does not eliminate the influence of the skew angle between the incident wave and the inspected surface; it is preferred when, owing to the mismatch between the reference measurement and the subsequent contact maps, the first approach leads to faulty results.

2.1.2 Nominal contact area

The load dependent nominal contact area $A_0(L)$ was evaluated by performing the following steps:

1. A threshold level of the reflection coefficient R_t is computed as:

$$R_t = R_{bg} - 3\sigma_{bg} \tag{3}$$

Where R_{bg} is the average reflection coefficient in the background and σ_{bg} the standard deviation in the same area. When computing R_{bg}, the contact patch is masked making use of an image segmentation algorithm that converts the reflection map in grey values and separate pixels into background and foreground. Therefore, this procedure is automated and the user's influence on the outcome of the processing operations is reduced.

2. A binary map is obtained by applying the threshold value R_t to the reflection map in such way that pixels having a reflection coefficient $R < R_t$ are considered belonging to the contact patch.
3. The load dependent nominal contact area $A_0(L)$ is estimated adding together the area of pixels belonging to the contact zone.

An example of the result of the binarization of the reflection map is shown in Figure 3.

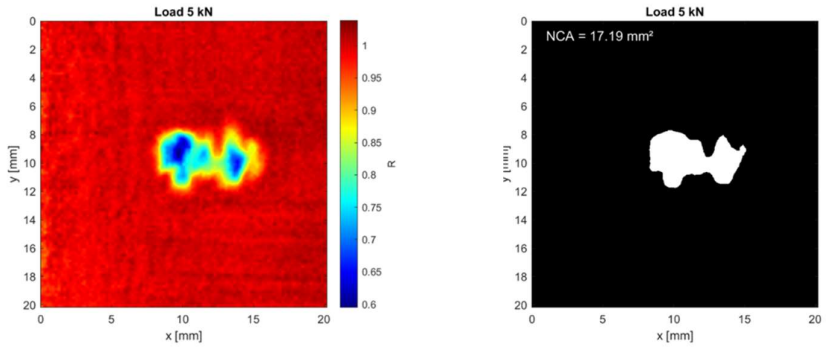

Figure 3 – Reflection map (on the left) beside the corresponding binary map (on the right). Result of the experiment conducted by pairing a ER7 wheel and a R260 rail under a force of 5 kN.

2.2 Finite element method

Finite Element Method (FEM) is a common numerical method for solving partial differential equations. Except for a few examples, these types of equations cannot be solved analytically and hence approximations, like *variational principles* [18] and the *Galerkin method* [19,20] must be applied. Thereby a solution is assumed, e.g., in the form of a polynomial, whose coefficients are then numerically determined. However, finding polynomial function as a solution for a system of complex geometry, which satisfies all boundary conditions can be difficult or even impossible. At this point, FEM comes into the numerical scheme with the basic idea to discretize the entire system into elements for each of which one assumes polynomial functions as solutions. This methodology has the advantage of allowing the usage of low order polynomial functions. Usually, these functions as solutions are identical for all elements and in terms of a mechanical boundary condition problem, they are often taken for the displacements. Accordingly, a system of algebraic equations is resulting for each element. These must be then assembled into a system of algebraic equations within the global coordinate system in the well-known form,

$$\boldsymbol{KU} = \boldsymbol{F}\,, \tag{4}$$

where $\boldsymbol{K}$ is the stiffness matrix representing the stiffness of the discretized geometry, $\boldsymbol{U}$ the vector of displacements containing known and unknow displacements, and $\boldsymbol{F}$ is the vector of the applied loads [21,22].

3 Experimental and numerical simulations

In this short section, both the experimental and numerical setups are introduced and explained. Related to the experimental part details concerning the data acquisition are also given. For the numerical simulations the considered geometry for the samples together with the type and quality of the applied discretisation are specified too.

3.1 Laboratory setup for ultrasonic contact area measurement

A 15 MHz broadband, longitudinal, focussed probe was used to characterize the static contact between wheel and rail specimens. The frequency response and the sound field parameters of the ultrasonic probe were determined following the ASTM E1065 standard procedures. A focal length of 89 mm and a spot diameter at -6 dB of 0.8 mm was measured. By performing the FFT of the waveform reflected from a spherical reflector, a central frequency of 15.6 MHz was found, a peak frequency of 15.1 MHz and a lower and upper frequency at -6 dB of 12.1 and 18.9 MHz.

The ultrasonic transducer, which carries both the function of transmitter and receiver, was connected to a Panametrics 5800PR pulser/receiver. The received signal was monitored by means of a Tektronix TDS3012B digital oscilloscope.

The loading frame use to conduct the static tests is schematically represented in Figure 4. The loading frame is made of a lower plate and an upper plate mounted on four M20 screws. On the upper plate there is a window for the access of the ultrasonic probe. The rail specimens are pressed against the bottom plate. The wheel specimens are supported by a thrust piece mounted on the load cell. The load is applied by means of a hydraulic jack. Since the immersion technique was used, a small tank for the coupling medium was sealed with the rail specimens.

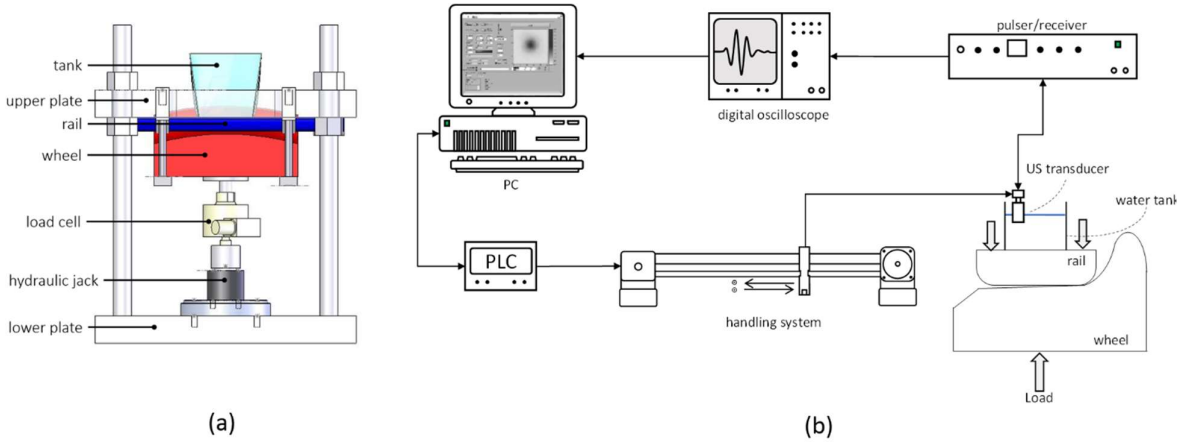

Figure 4 – (a) Frontal view of the loading system, (b) Schematic representation of the ultrasonic setup.

A two-axis scan system was used to move the ultrasonic probe over the region of interest. The movement is conferred by two stepper motors. The distance between probe and specimens was set manually and chosen to focus the ultrasonic beam to the contact interface. The position was controlled by reading on the oscilloscope the roundtrip time of the first reflection. The proper time of flight t for a desired distance d can be obtained as $t = 2d/c$, where c is the speed of sound in the coupling medium.

Both the probe's handling and the collection of the ultrasonic signal are managed by a home-made software developed in LabView. The dimension of the scanned area, the step length and the scanning speed are set by the user. The spatial resolution of the scan is determined by the step length and limited by the physical features of the probe. In this work, a step length of 0.2 mm was used, which results in a compromise between image resolution and acquisition speed. For each point of the scanned area, the peak-to-peak amplitude (in voltage) of the ultrasonic signal reflected from the contact interface is recorded, stored in a matrix, and saved in a text file. A false colour display of the matrix allows visual representation spatial distribution of the reflected signal (and thus of the shape of the contact area) as illustrated in Figure 2. This representation will be referred to as the *contact map*.

3.2 Constitutive model

The FE-model is built up by exactly following the laboratory setup and cutting out the interaction zone from real rails and wheels, namely from the widespread flat bottom rail UIC 60 and the wheel with the profile type S1002, respectively.

The nominal contact area of all wheel-rail pairs considered in the experiments is also calculated by a FEM simulation code written by using on the market well-established and widely applied ANSYS Mechanical software [23]. The approximate dimensions of the rail sample are 200 mm × 60 mm × 15 mm, whereas that of the wheel sample 200 mm × 120 mm × 80 mm. Their relative orientation and the Cartesian coordinate system with its origin in the middle of the wheel are all shown in Figure 5.

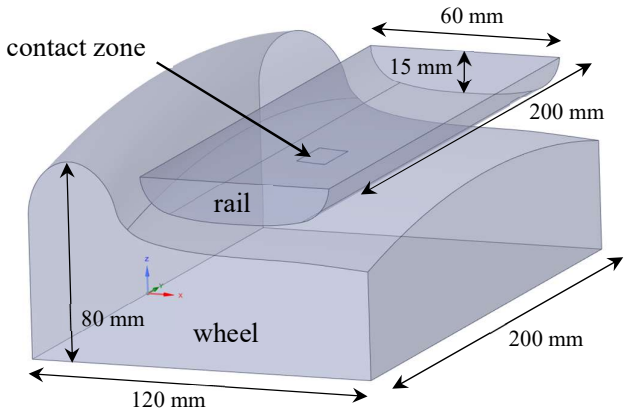

Figure 5- Setup of the 3D FEM model

Since in a preliminary study it was possible to estimate where the contact between wheel and rail will occur, an area of 10 mm × 20 mm was chosen including the entire contact zone, recall Figure 5. The interface in this contact zone is formed by two surfaces, namely one contact side on the wheel and another target side on the rail. An additional study subsequently performed, revealed that a size of 0.25 mm for the contact elements CONTA174 and the target elements TARGE170 are good compromises between computational performance and the accuracy in estimating the nominal contact area. The rest of both two bodies is discretized using the quadratic tetrahedral elements SOLID187. Altogether this results in a mesh of 74 372 elements with 100 003 nodes, Figure 6.

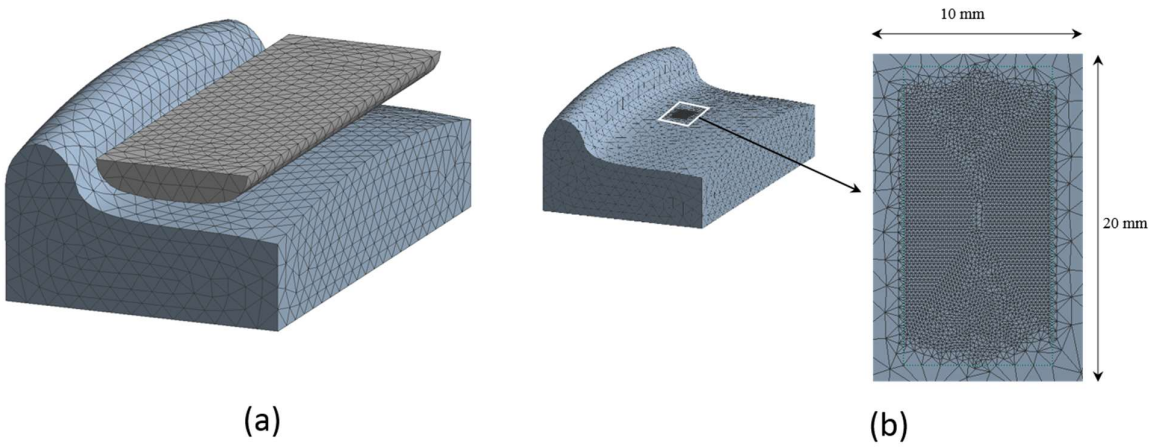

Figure 6- Discretized wheel and rail samples: (a) the coarse mesh on wheel and rail; (b) the fine mesh within the contact zone.

The boundary conditions applied to the discretized FEM-model are detailed in following. The bottom of the rail is kept fixed, whereas the displacements in the x- and y-directions of the wheel's surface having its normal vector directed along the y-direction were suppressed, such that the wheel could only move in the vertical z-direction. In the contact zone, the interaction between the wheel and rail is supposed to be frictionless. On the bottom of the wheel the load L is applied. This applied load is varied from 5 kN and to 60 kN in steps of 5 kN. In a preliminary study, it was shown that within this range of loads the materials involved are only linear elastically deforming. Note that steel grades ER7, ER9 and R260 have identical elastic material parameters, namely a Young's modulus of 200 GPa and Poisson's ratio 0.3. Therefore, a single numerical simulation covers all in the experiments tested cases.

4 Assessment of nominal contact area

As aforementioned, the ultrasonic experiments were carried out on wheel and rail samples which were directly cut from real pieces of wheels and rails as specified in Table 1. Each pairing was loaded from 5 kN to 60 kN in steps of 5 kN by keeping the samples all the time in contact over the entire loading period to avoid changes in their relative position. For each loading step an ultrasonic scan was performed. The measuring procedure was repeated three times, resulting in a total of six independent contact cases. After each set of experiments, the samples were unloaded, removed from the frame, and subsequently repositioned, in order to ensure the independent repetition of each measurement.

Since the relative position of wheel and rail directly affects the size and shape of their nominal contact area, the repositioning was performed by using markers placed on both samples and on the loading frame, namely a sheet of graph paper was attached to the transversal flat surface of the wheel whereas the upper part of the test rig was equipped with a plumbline vertically aligned to the side edge of the rail. Thus, the relative position of the wheel and rail together with the loading frame was determined by reading the position of the plumbline on the graph paper.

Pairing	Type		Conditions		Hardness [HBW]	
	Wheel	Rail	Wheel	Rail	Wheel	Rail
1	ER7 #1	R260 #1	worn	new	235	260
2	ER9 #2	R260 #1	worn	new	235	260

Table 1 – Contact test specifications.

4.1 Improved image-processing

Figure 7 (a) and (b) show the results of the binarization procedure for assessing the size and shape of the contact patch for the whole set experiments on the wheel-rail pairings listed in Table 1. The values of the measured nominal contact area are listed in Table 2.

The results of the three repetitions are shown as contour plots stacked in a single image for an easier comparison. The visual inspection of the image set reveals that the whole experimental procedure is characterized by high accuracy and repeatability. The shape of the contact patches appears to be far from the regular ellipse predicted by the Hertzian theory, and the edges are irregular and influenced by the level of load. Irregularities on the contact patch shape are caused by irregularities of the specimen's surfaces coming into contact. Such behaviour is not surprising since the contact pairs are made by coupling used wheel and rail cuts. Also, for each load, the shapes of the three contours are slightly different. Despite of all these tiny differences, it can be stated that most of irregularities are detected within the independent measurements for each load.

Since these irregularities are directly related to the surface ones, it can be concluded that the applied repositioning protocol was successful and satisfactory. This still has an observable impact on the variability of A_0, recall Table 2.

On the other hand, it is noticeable that the morphology of the contact patch is "recognizable" for the three independent measurements, thus confirming that

- the ultrasonic method is capable to correctly measure the actual shape of the contact patch;
- the repositioning procedure allows to ensure that the contact occurs in the same region of the surface specimens in the whole set of independent experiments;
- the proposed post processing procedures for the data binarization is reliable and allows to assess the actual shape of the contact patch.

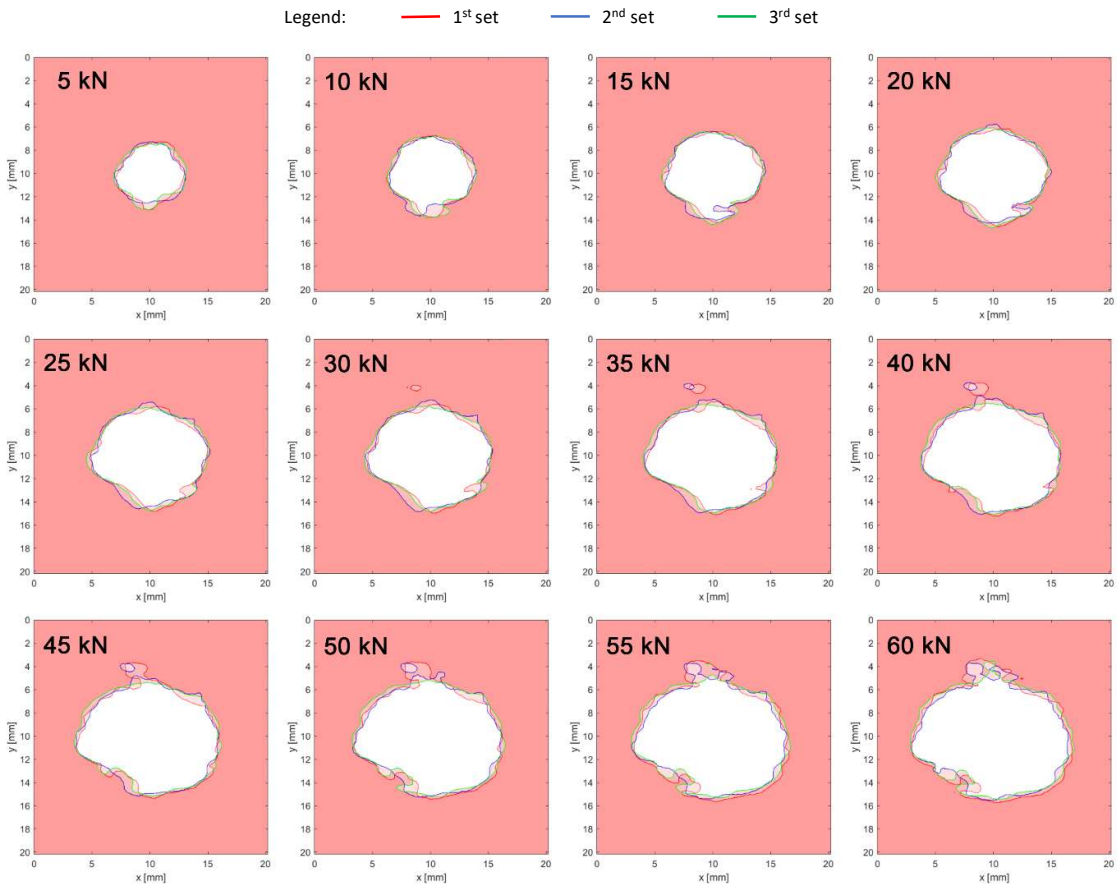
Legend:
1st set
2nd set
3rd set
5 kN
10 kN
15 kN
20 kN
25 kN
30 kN
35 kN
40 kN
45 kN
50 kN
55 kN
60 kN
x [mm]
y [mm]

(a)

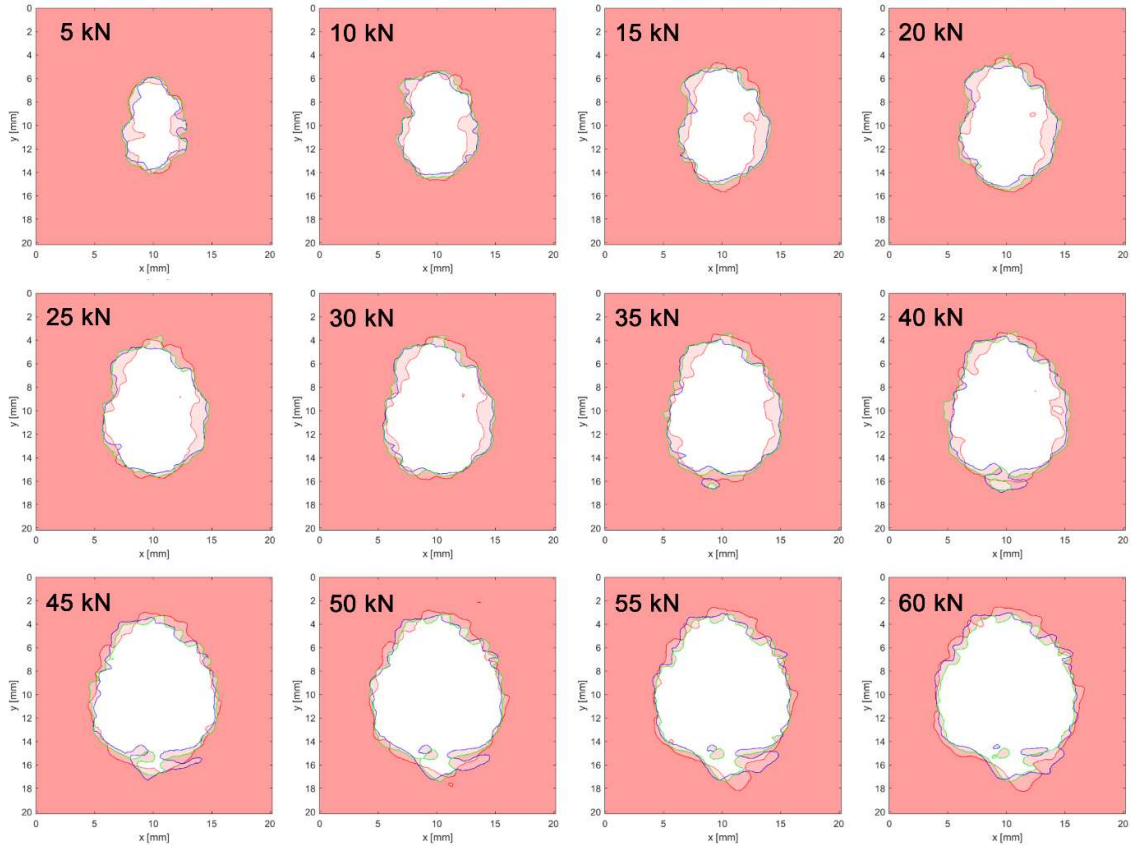

(b)

Figure 7 – Binary contact maps for increasing loads. Comparison between the three series of experiments: (a) Rail R260 new-Wheel ER7 worn; (b) Rail R260 new-Wheel ER9 worn.

4.2 Load dependence

	$A_0(L)$ [mm²]					
	Wheel ER7-Rail R260			Wheel ER9-Rail R260		
Load [kN]	1st	2nd	3rd	1st	2nd	3rd
5	17.19	21.9	27.76	20.56	19.85	22.60
10	33	37.21	43.67	33.25	30.48	35.68
15	43.23	49.58	55.04	42.78	41.23	46.02
20	52.83	59.48	64.5	51.14	49.94	56.11
25	61.56	68.13	72.87	58.33	58.90	62.94
30	68.63	75.96	80.1	65.54	67.04	69.28
35	75.55	83.23	86.4	73.17	73.93	76.53
40	82.16	91.7	93.83	80.6	80.00	82.90
45	92.13	98.37	97.51	89.06	84.85	88.71
50	103.31	108.76	105.58	95.88	89.76	95.17
55	111.88	116.86	110.55	107.28	95.93	102.32
60	120.27	123.27	113.17	114.6	101.64	109.45

Table 2 – Load-dependent nominal contact area obtained for two different pairings in three measurements.

The load-dependent nominal contact area $A_0(L)$ of three experimental sets and the two pairings listed in Table 2 are also shown in Figure 8 (a) and (b), where these data are fitted to the power law,

$$A_0(L) = \alpha L^{\beta}\,. \tag{5}$$

Here the load independent amplitude α and exponent β are fitting parameters which could be directly determined, e.g., by using a least-square minimization. However, when normalizing both independent and dependent variables dividing them by to these quantities related reference values, Equation (5) is written as

$$\frac{A_0(L)}{A_0(L_{ref})} = \gamma\left(\frac{L}{L_{ref}}\right)^{\beta}. \tag{6}$$

Here and in the following, for the load $L_{\mathrm{ref}} = 5$ kN is considered as reference value, and accordingly the other reference quantity is so immediately fixed as $A_0(L_{\mathrm{ref}})$, namely it is to this reference load L_{ref} corresponding nominal contact area. Now, taking the natural logarithm of Equation (6),

$$\ln\left(\frac{A_0(L)}{A_0(L_{ref})}\right) = \ln(\gamma) + \beta\ln\left(\frac{L}{L_{ref}}\right), \tag{7}$$

this is in a proper form to apply linear regression for providing both dimensionless fitting parameters γ and β. Note that the parameter γ it can be seen as a measure of validity for the load independence of the amplitude α in Equation (5) and hence it is expected for γ to have its value near the unity when the power-law dependence on load of the nominal contact area indeed holds.

The calculated values of parameters γ and β, together with the respective standard deviations σ_γ and σ_β and the coefficient of determination R^2 are all listed in Table 3, which also includes the amplitude α calculated as

$$\alpha = \gamma \cdot \frac{A_0(L_{ref})}{L_{ref}^{\beta}}. \tag{8}$$

As it can be seen in this Table 3, the obtained validity parameter γ is really very close to unity by lying within the range between 0.906 and 1.09, which together with the coefficient of determination R^2 over 99.4 %, are clearly proving the validity of Equation (5), namely that the nominal contact area shows a power-law dependence on the applied load.

Pairing		$A_0(L_{ref})$ [mm²]	γ	σ_γ	β	σ_β	R^2 [%])	α [mm² kN$^{-\beta}$]
Wheel ER7-Rail R260	1st	17.19	1.048	0.058	0.755	0.026	99.47	5.35
	2nd	21.90	1.044	0.029	0.675	0.013	99.82	7.72
	3rd	27.76	1.090	0.025	0.539	0.011	99.79	12.72
	mean	22.28	1.061	0.037	0.656	0.016	99.69	8.59
Wheel ER9 Rail R260	1st	20.56	0.906	0.048	0.720	0.025	99.43	5.85
	2nd	19.85	1.036	0.028	0.646	0.013	99.82	7.28
	3rd	22.60	1.021	0.022	0.619	0.010	99.86	8.52
	mean	21.00	0.988	0.033	0.661	0.016	99.70	7.21

Table 3 – The dimensionless fitting parameters γ and β from Equation (7) determined by using linear regression together with their so obtained standard errors σ_γ and σ_β, and the coefficient of determination R^2, when the reference nominal contact area $A_0(L_{ref})$ is that corresponding to the load L_{ref} = 5 kN. The amplitude α entering Equation 5 is calculated using g and Equation (8).

The exponent β is found in Table 3 within the range between 0.539 and 0.755 and having average values of 0.661 and 0.656. It is interesting to observe that even though the contact maps originate from three independent measurements and hence they are substantially superimposable in terms of geometrical extension and morphology, the value of β varies almost 30%. On the other hand, the average value of the exponent β is surprisingly 2/3 as predicted by the Hertzian contact model! In view of the highly elliptical form of the experimentally estimated nominal contact area, recall Figure 10, one could speculate in saying that for the wheel/rail contacts in average the elliptical Hertzian contact model holds [24]. Strictly speaking, however, this cannot be fully accepted, since we observed a strong load dependence of ellipticity in contradiction with the elliptical Hertzian contact model as applied for wheel/rail contacts [25], where an ellipticity only depends on the initial curvatures. Now, one could argue that the elliptical Hertzian contact model for wheel-rail pairings is not really the state-of-the-art view on these contacts, since the so-called simple double-elliptic contact (SDEC) [26] implemented also as an extension to the software FASTSIM [27], seems to be more adequate. Nevertheless, we cannot see that non-ellipticity [28] in our measured data on the nominal contact area which is the precondition of applying SDEC as contact model. Therefore, we are concluding that the elliptical Hertzian contact model could still serve as a first and robust approach for starting interpreting either experimental or numerical wheel-rail contact data. Even more, analysing the exponent β, recall Table 2, in terms of the hardening exponent κ and the homogeneity degree of the contact's shape d, it is reconfirmed within the similarity approach introduced in Ref. [29] and applied in Ref. [30], that here the wheels and rails in contact are elastically deformed (κ = 1) yielding an either circular or elliptical nominal contact area (d = 2). This seems to also support our latter statement elegantly about the applicability of the elliptical Hertzian model.

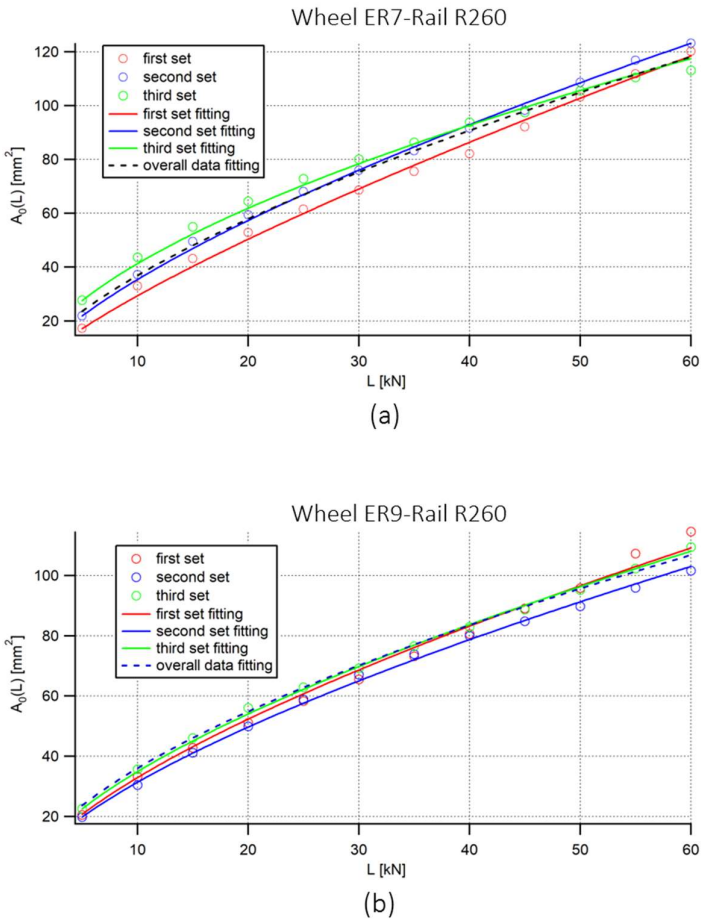

Figure 8 – Load-dependent nominal contact area $A_0(L)$ obtained for two different pairings in three measurements fitted with power-law dependence from Equation (5).

4.3 Computed results

For a better understanding the curiosities observed within the modelling of the measured experimental data, also FEM-calculations are performed. In Figure 9 – *(a) Contact pressure for the minimum and maximum load applied to the wheel-rail pairing in Figures 8, and (b) the FEM-calculated load-dependent nominal contact area $A_0(L)$, see filled squares within, together with its power-law model as given by Equation 6 represented by the solid line.* (a), the distribution of the contact pressure is depicted for the lowest and the highest load considered. It is clearly visible that the numerically simulated shape of the contact is more elliptical than seen in the experiment in Figure 7. This can be explained by the fact that the curvature of the rail is not the same in the x- and y-directions, i.e., in the contact zone is the radius in x-direction 300 mm and in y-direction infinite. Comparing in Figure 12 (b) the FEM-calculated load-dependent nominal contact area with a load-dependence in Equation (6), when this is obtained via linear regression from Equation (7) taken for L_{ref} = 5 kN, and $A_0(L_{ref}) = 13.342\ \mathrm{mm}^2$, a very high validity γ = 0.995 and an almost Hertzian-exponent β = 0.654 are resulting with a perfect coefficient of determination $R^2 = 1.000$. This again is reconfirming what it was also

concluded in Section 4.2, namely that the Hertzian contact model could be a first guess for the wheel-rail case too.

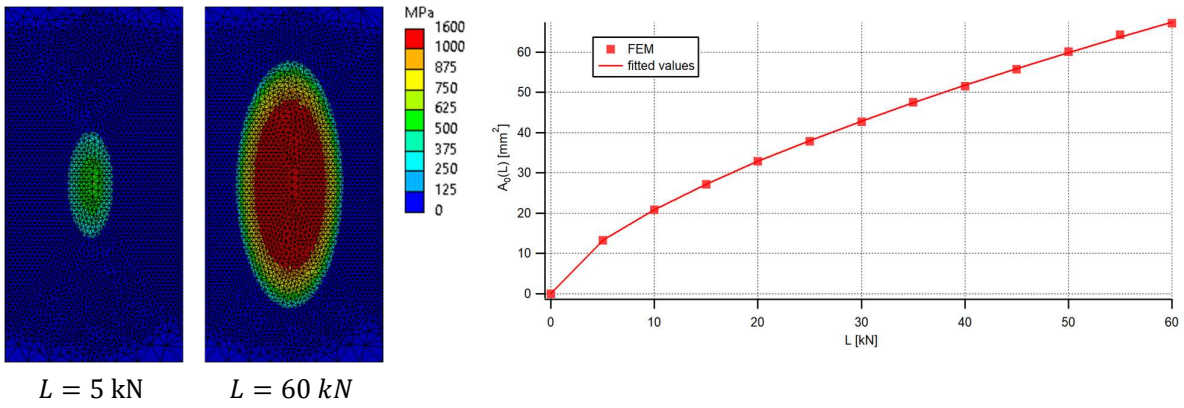

$L = 5$ kN $L = 60\ kN$

(a) (b)

Figure 9 – *(a) Contact pressure for the minimum and maximum load applied to the wheel-rail pairing in Figures 8, and (b) the FEM-calculated load-dependent nominal contact area $A_0(L)$, see filled squares within, together with its power-law model as given by Equation 6 represented by the solid line.*

4.4 Comparison with data from literature

A comparison of our experimental and numerical results with those available in the literature could be somewhat challenging, as published data are obtained in other conditions concerning geometry, load, materials, and so on. In this perspective, the assessment of the trend based on the parameters introduced in Equation (7) represents a huge step forward for setting a common basis for the comparison.

Upon these considerations, literature dealing with the wheel/rail contact problem are analysed, focusing only on papers which provide measured and/or calculated nominal contact areas. Furthermore, because most of publications are not focused on the relationship between the nominal contact area and the applied load, only a limited number of papers, mainly experimental ones, could serve the comparison with our results. In addition, these few data are found inhomogeneous in terms of the wheel/rail geometry, use conditions, applied load range besides of differing in the applied experimental techniques. Therefore, only a subset of gathered papers, namely those providing data on the contact area for different (at least three) load levels, are here considered for a comparison with our results.

A printed image of the contact patch originated by locomotive wheel and rail was obtained in [31] by inserting thin sheets of carbon and ordinary paper between the two elements. They measured the area of the patch for different load levels. The same principle of inserting between wheel and rail a thin sheet sensitive to the exerted pressure is exploited in Ref. [32] by using a Fuji Prescale film of various sensitivities. As largely discussed above in this paper, the ultrasonic reflectometry method has been extensively used in the past two decades for the assessment of the contact conditions between railways wheel and rail, and the area of the contact zone for various loads, see Refs. [11], [33] and [34].

For all these papers, values of the nominal contact area and the applied load are collected for applying the same procedure as described in Section 4.2 to calculate the dimensionless parameters β and γ. In case of papers providing graphically their results the public domain software ImageJ was taken to extract the numerical values. The so obtained results are listed in **Errore. L'origine riferimento non è stata trovata.**, where also the reference load L_{ref} is given, since it is not the same for all data sets.

Contact / technique [Reference]	L_{ref} **[kN]**	$A(L_{ref})$ **[mm²]**	γ	σ_γ	β	σ_β	R^2 **[%]**	α **[mm² kN$^{-\beta}$]**
New / carbon paper [31]	10.9	935.4	0.925	0.009	0.445	0.014	98.78	298.83
Worn / carbon paper [31]	10.8	779.2	0.902	0.007	0.491	0.017	98.54	218.64
Worn / ultrasonic [33]	40.0	134.9	0.984	0.026	0.531	0.081	97.72	18.751
New / theoretical [11]	45.0	56.5	1.001	0.0007	0.660	0.0037	99.98	4.5807
New / ultrasonic [11]	45.0	86.2	0.981	0.007	0.439	0.043	94.50	15.895
New / Fuji film “High” [32]	2.0	12.1	0.968	0.021	0.518	0.053	97.99	8.1782
New / Fuji film “Superhigh” [32]	2.0	10.6	0.988	0.007	0.583	0.017	99.64	6.9962
New / ultrasonic [34]	1.5	4.3	1.027	0.012	0.675	0.019	98.72	3.4045

Table 4 – As in Table 3, but for data extracted from literature and setting the reference for the applied load at its minimum value.

The parameter γ introduced in Equation 6 for quantifying the validity of the power-law dependence on load of the nominal contact area, recall Equation 5, also works for the experimental data from the literature, see the γ, σ_γ, and R^2 in Table 4. Even more, this γ can distinguish between the application of carbon and Fuji films and points out the high accuracy of ultrasound techniques for measuring pressure distributions and/or nominal contact area.

The exponent β is another general-purpose quantity aiming the comparison of our ultrasound measurements and numerical simulations with the similar data found in the literature. As it can be seen in Table 4, this β is in the range we got too, expect the theoretical result according Ref. [11] which coincides exactly with the well-known Hertzian 2/3 exponent.

As before in Section 4.2, the amplitude α cannot be really considered for a direct comparison of various measurements and/or numerical calculations because it is strongly depending on the peculiarities of the used wheel-rail pairings and the loading conditions. Apart from all these, its unit is very complex, which also depends on the exponent β, makes α even in Table 3 hardly comparable for different sets.

5 Conclusions

In this work we studied the contact area of real wheel-rail pairings taken from practical application. The nominal contact area under realistic load conditions was measured via scanning an ultrasonic probe over the contact region. Experimental measurements were aided by numerical FEM simulations of the contact. Following main conclusions can be drawn from the gained results:

- The measurement of the real contact area with ultrasonic scanning was repeatable and reliable. This was achieved by an improved post processing procedure, based on the analysis of the background

signal, which is fully automatic in order to avoid operator influence. The experimental results showed a load dependence of the contact ellipticity.

- The dependence of the nominal contact area with the load was studied assuming a power law of exponent β. The hypothesis was investigated by performing linear regression of the experimental data (prior normalization and logarithmic transformation)
- Two dimensionless quantities were introduced, namely γ measuring the validity of the power-law load dependence of the nominal contact area $A_0(L)$, and exponent β fixing how strongly is depending A_0 on the load.
- β coincides in average with the well-known Hertzian 2/3 exponent, although the preconditions for the applicability of even the elliptical Hertzian contact model are not fulfilled by our wheel-rail pairings, e.g., the calculated ellipticity of the measured nominal contact area is definitely load dependent.

In a forthcoming work, the authors intend to apply the same ultrasound technique together with the improved image-processing numerical tool for studying the load dependence of the real contact area, i.e., when both the roughness and waviness of contacting surfaces are considered within the wheel-rail contacts.

6 Acknowledgement

This work was funded by the Austrian COMET-Program (project InTribology, no. 872176) via the Austrian Research Promotion Agency (FFG) and the Provinces of Niederösterreich and Vorarlberg and was carried out within the “Excellence Centre of Tribology” (AC2T research GmbH).

7 References

1. I. Stratmann, J. Goersch, C. Schindler, "Overview of methods to identify the static normal wheel-rail contact", Proceedings of the Institution of Mechanical Engineers, Part F: Journal of Rail and Rapid Transit. 2022;236(7):783-792. https://doi.org/10.1177/09544097211042487.
2. M. Pau, F. Aymerich, and F. Ginesu, "Ultrasonic Measurements of Nominal Contact Area and Contact Pressure in a Wheel-Rail System," *Proceedings of the Institution of Mechanical Engineers, Part F: Journal of Rail and Rapid Transit* 214, no. 4 (July 1, 2000): 231–43, https://doi.org/10.1243/0954409001531333.
3. M. Pau, F. Aymerich, and F. Ginesu, "Distribution of Contact Pressure in Wheel–Rail Contact Area," *Wear* 253, no. 1–2 (2002): 265–74, https://doi.org/10.1016/S0043-1648(02)00112-6.
4. M.B. Marshall et al., "Ultrasonic Characterisation of a Wheel/Rail Contact," in *Tribology Series*, vol. 43 (Elsevier, 2003), 151–58, https://doi.org/10.1016/S0167-8922(03)80043-3.
5. H. G. Tattersall, "The Ultrasonic Pulse-Echo Technique as Applied to Adhesion Testing," *Journal of Physics D: Applied Physics* 6, no. 7 (May 1, 1973): 819–32, https://doi.org/10.1088/0022-3727/6/7/305.
6. R.S. Dwyer-Joyce and B.W. Drinkwater, "In Situ Measurement of Contact Area and Pressure Distribution in Machine Elements," *Tribology Letters* 14, no. 1 (2003): 41–52, https://doi.org/10.1023/A:1021766216019.
7. F. Aymerich and M. Pau, "Assessment of Nominal Contact Area Parameters by Means of Ultrasonic Waves," *Journal of Tribology* 126, no. 4 (October 1, 2004): 639–45, https://doi.org/10.1115/1.1760764.
8. E07 Committee, "Practice for Evaluating Characteristics of Ultrasonic Search Units" (ASTM International), accessed July 14, 2023, https://doi.org/10.1520/E1065_E1065M-20.
9. M. Pau, "Ultrasonic Waves for Effective Assessment of Wheel-Rail Contact Anomalies," *Proceedings of the Institution of Mechanical Engineers, Part F: Journal of Rail and Rapid Transit* 219, no. 2 (March 1, 2005): 79–90, https://doi.org/10.1243/095440905X8808.
10. M. Pau, B. Leban, and A. Baldi, "Simultaneous Subsurface Defect Detection and Contact Parameter Assessment in a Wheel–Rail System," *Wear* 265, no. 11–12 (2008): 1837–47, https://doi.org/10.1016/j.wear.2008.04.030.
11. M. B. Marshall et al., "Experimental Characterization of Wheel-Rail Contact Patch Evolution," *Journal of Tribology* 128, no. 3 (July 1, 2006): 493–504, https://doi.org/10.1115/1.2197523.
12. S. Fukagai et al., "Using Active Ultrasonics to Measure Wheel-Rail Contact During a Running-in Period," *International Journal of Railway Technology* 7, no. 3 (September 12, 2018): 1–20, https://doi.org/10.4203/ijrt.7.3.1.
13. L. Zhou et al., "Real-Time Measurement of Dynamic Wheel-Rail Contacts Using Ultrasonic Reflectometry," *Journal of Tribology* 141, no. 6 (June 1, 2019): 061401, https://doi.org/10.1115/1.4043281.
14. M. Schoenberg, "Elastic Wave Behavior across Linear Slip Interfaces," *The Journal of the Acoustical Society of America* 68, no. 5 (1980): 1516–21, https://doi.org/10.1121/1.385077.
15. J. Królikowski, J. Szczepek, and Z. Witczak, "Ultrasonic Investigation of Contact between Solids under High Hydrostatic Pressure," *Ultrasonics* 27, no. 1 (1989): 45–49, https://doi.org/10.1016/0041-624X(89)90008-5.

16. M. Schirru, M. Varga, "A Review of Ultrasonic Reflectometry for the Physical Characterization of Lubricated Tribological Contacts: History, Methods, Devices, and Technological Trends", Tribology Letters, 70 (4), art. no. 129 (2022), https://doi.org/10.1007/s11249-022-01670-8.
17. B.W. Drinkwater, R.S. Dwyer-Joyce, and P. Cawley, "A Study of the Interaction between Ultrasound and a Partially Contacting Solid—Solid Interface," *Proceedings of the Royal Society of London. Series A: Mathematical, Physical and Engineering Sciences* 452, no. 1955 (December 31, 1996): 2613–28, https://doi.org/10.1098/rspa.1996.0139.
18. W. Ritz, "Über eine neue Methode zur Lösung gewisser Variationsprobleme der mathematischen Physik," Journal für die reine und angewadnte Mathematik, no. 135, pp. 1-61, 1909.
19. B. Galerkin, "Sterzhni i plastiny. Ryady v nekotorykh voprosakh uprugogo ravnovesiya sterzhnei i plastin (Rods and plates series occuring in some problems of elastic equilibrium of rods and plates)," Vestnik Inzhenerov i Tekhnikov, vol. 19, pp. 897-908, 1915.
20. C. B. Biezeno and R. Grammel, Lösungsmethoden, Berlin, Heidelberg: Springer, 1939, pp. 123-225.
21. O. Zienkiewicz, R. Taylor and J. Zhu, "The Finite Element Method: Its Basis and Fundamentals" (Elsevier, 2013), https://doi.org/10.1016/C2009-0-24909-9.
22. B. Klein, FEM - Grundlagen und Anwendungen der Finite-Element-Methode im Maschinen- und Fahrzeugbau (10. Auflage), Wiesbaden: Springer Vieweg, 2015.
23. Ansys® Mechanical 2023 R1.
24. J. Antoine, C. Visa, C. Sauvey, G. Abba "Approximate Analytical Model for Hertzian Elliptical Contact Problems." ASME. J. Tribol. July 2006; 128(3): 660–664. https://doi.org/10.1115/1.2197850
25. F.D. Fischer, M. Wiest "Approximate Analytical Model for Hertzian Elliptical Wheel/Rail or Wheel/Crossing Contact Problems." ASME. J. Tribol. October 2008; 130(4): 044501. https://doi.org/10.1115/1.2958074
26. B. Liu, B. Fu, S. Bruni "Generalisation of the linear theory of rolling contact to a single double-elliptic contact region and its application to solve non-Hertzian contact problems using extended FASTSIM" (2022) Vehicle System Dynamics, International Journal of Vehicle Mechanics and Mobility, Volume 61, 2023, Issue 10. https://doi.org/10.1080/00423114.2022.2113808
27. J.J. Kalker "A Fast Algorithm for the Simplified Theory of Rolling Contact", Vehicle System Dynamics, International Journal of Vehicle Mechanics and Mobility, Volume 11, 1982 - Issue 1. https://doi.org/10.1080/00423118208968684
28. Y. Chen, Y. Sun, W. Ding, P. Wang "Assessing the fast non-Hertzian methods for wheel-rail rolling contact integrated in the vehicle dynamics simulation" Proceedings of the Institution of Mechanical Engineers, Part F: Journal of Rail and Rapid Transit. 2023;237(3):371-384. doi:10.1177/09544097221113462
29. F.M. Borodich "The hertz frictional contact between nonlinear elastic anisotropic bodies (the similarity approach)", (1993) International Journal of Solids and Structures, 30 (11), pp. 1513-1526. https://doi.org/ 10.1016/0020-7683(93)90075-I
30. F.M. Borodich et al. "Wear and abrasiveness of hard carbon-containing coatings under variation of the load", Surface and Coatings Technology, (2004) Vol.179, Issue 1, 2, pp. 78-82. https://doi.org/10.1016/S0257-8972(03)00797-7
31. H.I. Andrews, "The Contact between a Locomotive Driving Wheel and the Rail," *Wear* 2, no. 6 (1959): 468–84, https://doi.org/10.1016/0043-1648(59)90161-9.
32. A. Radmehr et al., "Wheel-Rail Contact Patch Geometry Measurement and Shape Analysis Under Various Loading Conditions," in *2020 Joint Rail Conference* (2020 Joint Rail Conference, St. Louis,

Missouri, USA: American Society of Mechanical Engineers, 2020), V001T13A005, https://doi.org/10.1115/JRC2020-8042.

33. H. Brunskill et al., "An Evaluation of Ultrasonic Arrays for the Static and Dynamic Measurement of Wheel–Rail Contact Pressure and Area," *Proceedings of the Institution of Mechanical Engineers, Part J: Journal of Engineering Tribology* 234, no. 10 (2020): 1580–93, https://doi.org/10.1177/1350650120919889.

34. M. Pau, "Estimation of Real Contact Area in a Wheel-Rail System by Means of Ultrasonic Waves," *Tribology International* 36, no. 9 (2003): 687–90, https://doi.org/10.1016/S0301-679X(03)00014-8.